
A systematic study of Galactic infrared bubbles along the Galactic plane with AKARI and Herschel. II. Spatial distributions of dust components around the bubbles.

Misaki HANAOKA¹, Hidehiro KANEDA¹, Toyoaki SUZUKI¹, Takuma KOKUSHO¹, Shinki OYABU¹, Daisuke ISHIHARA¹, Mikito KOHNO¹, Takuya FURUTA¹, Takuro TSUCHIKAWA¹ and Futoshi SAITO¹

¹Graduate School of Science, Nagoya University, Furo-cho, Chikusa-ku, Nagoya 464-8602, Japan

*E-mail: hanaoka@u.phys.nagoya-u.ac.jp, kaneda@u.phys.nagoya-u.ac.jp

Received (reception date); Accepted (acceptation date)

Abstract

Galactic infrared (IR) bubbles, which can be seen as shell-like structures at mid-IR wavelengths, are known to possess massive stars within their shell boundaries. In our previous study, Hanaoka et al. (2019) expanded the research area to the whole Galactic plane ($0^\circ \leq l \leq 360^\circ$, $|b| \leq 5^\circ$) and studied systematic differences in the shell morphology and the IR luminosity of the IR bubbles between inner and outer Galactic regions. In this study, utilizing high spatial-resolution data of AKARI and WISE in the mid-IR and Herschel in the far-IR, we investigate the spatial distributions of dust components around each IR bubble to discuss the relation between the star-formation activity and the dust properties of the IR bubbles. For the 247 IR bubbles studied in Hanaoka et al. (2019), 165 IR bubbles are investigated in this study, which have the Herschel data ($|b| \leq 1^\circ$) and known distances. We created their spectral energy distributions on a pixel-by-pixel basis around each IR bubble, and decomposed them with a dust model consisting of polycyclic aromatic hydrocarbons (PAHs), hot dust, warm dust and cold dust. As a result, we find that the offsets of dust heating sources from the shell centers in inner Galactic regions are systematically larger than those in outer Galactic regions. Many of the broken bubbles in inner Galactic regions show large angles between the offset and the broken shell directions from the center. Moreover, the spatial variations of the PAH intensity and cold dust emissivity around the IR bubbles in inner Galactic regions are larger than those in outer Galactic regions. We discuss these results in light of the interstellar environments and the formation mechanism of the massive stars associated with the IR bubbles.

Key words: infrared: ISM — ISM: bubbles — star: formation — star: massive

1 Introduction

There are a large number of Galactic infrared (IR) bubbles existing along the Galactic plane. They have shell-like structures, which can be clearly seen at mid-IR wave-

lengths. Churchwell et al. (2006, 2007) cataloged 591 IR bubbles which are located in inner Galactic regions ($|l| \leq 65^\circ$, $|b| \leq 1^\circ$), using the $8 \mu\text{m}$ band images of the Galactic Legacy Infrared Mid-plane Survey Extraordinaire (GLIMPSE: Benjamin et al. 2003; Churchwell et al. 2009)

program with Spitzer. In our previous study, Hanaoka et al. (2019) expanded the research area to the whole Galactic plane ($0^\circ \leq l \leq 360^\circ$, $|b| \leq 5^\circ$) and newly found 175 IR bubbles with large angular radii $R > 1'$ using the $9 \mu\text{m}$ band images of the all-sky surveys with AKARI (Murakami et al. 2007; Ishihara et al. 2010).

The shell-like structure associated with the IR bubbles can be seen clearly in the Spitzer $8 \mu\text{m}$ and AKARI $9 \mu\text{m}$ band images. These band intensities are expected to be dominated by polycyclic aromatic hydrocarbon (PAH) emission from photodissociation regions (PDRs). PAHs are easily photodissociated by strong ultraviolet (UV) radiation ($\geq 13.6 \text{ eV}$), thus they can hardly exist in H II regions. The IR bubbles are expected to possess the spherical shell structure formed on the edge of the H II region. Ionizing gases are distributed within the shell structures, producing the mid-IR continuum emission which mostly traces hot dust in H II regions (Deharveng et al. 2010). Hanaoka et al. (2019) confirmed that 97% of the 247 IR bubbles along the Galactic plane show diffuse hot dust emission within the shell boundaries using the AKARI $18 \mu\text{m}$ images. Thus, most of the IR bubbles possess massive stars within their shell structures.

In order to understand the massive star formation, triggered star-formation mechanisms have been discussed. Typical massive star-formation mechanisms are triggered by expansion of the H II regions and cloud-cloud collision (CCC) (e.g., Elmegreen 1998; Zinnecker & Yorke 2007; Deharveng et al. 2010). The former mechanism compresses the interstellar media (ISM) at the edges of the H II regions and dense clumps by radiation from the pre-existing massive stars (e.g., Deharveng et al. 2010; Dale et al. 2007; Gritschneider et al. 2009). The CCC mechanism triggers a massive star formation on the collision surface between two molecular clouds (Habe & Ohta 1992). A collision of two molecular clouds having different velocities makes an intermediate velocity component at the collision surface, which is seen as a broad bridge feature on the position-velocity map (e.g., Hawarth et al. 2015; Takahira et al. 2018).

In the previous study, Hattori et al. (2016) classified the IR bubbles cataloged in Churchwell et al. (2006, 2007) by the shell morphologies according to the quantitative criteria established in their study. They also estimated the IR flux densities and the spatial distributions of dust emission in and around each IR bubble using the 9 , 18 , 65 , 90 , 140 and $160 \mu\text{m}$ band images of the AKARI all-sky surveys. Then, they found that large broken bubbles tend to have higher total IR luminosities, lower fractional luminosities of the PAH emission and dust heating sources located nearer to the shells. Based on these results, Hattori et

al. (2016) suggested that many of the large broken bubbles might have been formed by the CCC mechanism. Hanaoka et al. (2019) expanded the study of Hattori et al. (2016) to the whole Galactic regions ($0^\circ \leq l \leq 360^\circ$, $|b| \leq 5^\circ$) and newly found 175 IR bubbles. Hanaoka et al. (2019) obtained the shell radii, the covering fractions (CFs) of the shells and the IR luminosities of 247 IR bubbles with large angular radii $R > 1'$ including the IR bubbles studied by Hattori et al. (2016). They found that there are systematic differences in the global IR properties of the IR bubbles between inner and outer Galactic regions and suggested that the results are interpreted by the interstellar environments around the IR bubbles and the star-formation mechanisms of the central massive stars. However, Hanaoka et al. (2019) did not perform a spatially-resolved study of the IR properties.

In this study, we investigate the spatial distributions of dust components of the IR bubbles to discuss the relation between the star-formation activity and the dust properties. By using high spatial resolution data of Herschel Space Observatory (Pilbratt et al. 2010) whose resolution is comparable to that of the AKARI $9 \mu\text{m}$ band image tracing the PAH emission, the spatial variations of the dust properties in the IR bubbles are discussed in more detail. The mid-IR wavelength data observed by the Wide-field Infrared Survey Explorer (WISE: Wright et al. 2010) are also added to estimate a hot dust ($> 100 \text{ K}$) component, which traces the environments closer to massive stars. Then, we obtain the overall properties of the IR bubbles along the whole Galactic plane and discuss the effects of the massive stars and interstellar environments on the properties of the IR bubbles in inner and outer Galactic regions.

2 Observation and data analysis

To investigate the local infrared properties of the IR bubbles studied by Hanaoka et al. (2019), we used AKARI, Herschel and WISE photometric data. The AKARI mid-IR all-sky surveys were carried out in two photometric bands (the central wavelengths are 9 , $18 \mu\text{m}$; Onaka et al. 2007), which covered more than 90% of the whole sky (Ishihara et al. 2010). The Herschel infrared Galactic Plane Survey (Hi-GAL: Molinari et al. 2010, 2016) is an unbiased photometric survey of the Galactic plane ($0^\circ \leq l < 360^\circ$, $|b| < 1^\circ$) at 70 , 160 , 250 , 350 and $500 \mu\text{m}$ wavelengths (Poglitsch et al. 2010; Griffin et al. 2010). All the Hi-GAL images are publicly available in the Herschel Science Archive¹, and the high-quality data of Hi-GAL

¹ Herschel Science Archive <http://archives.esac.esa.int/hsa/whsa/>

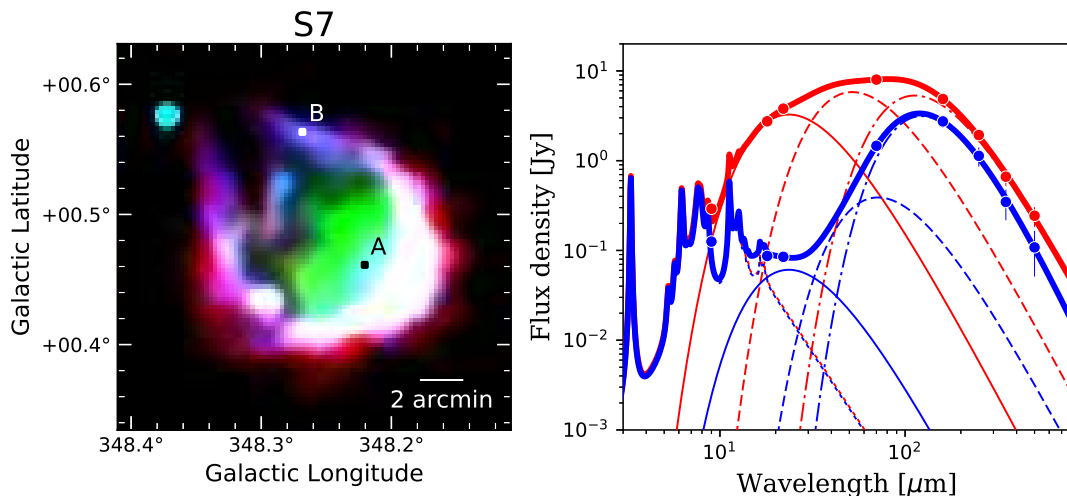


Fig. 1. Examples of the local SED-fitting results for one of our sample IR bubbles, S7 (named “RCW 120” by Rodgers et al. 1960). The left panel shows the composite image of S7, consisting of AKARI 9 μm , 18 μm and the Herschel 160 μm band images in blue, green and red, respectively. The right panel shows the fitting results of the local SED at the positions denoted in the left panel, the red and blue curves for “A” and “B”, respectively. The local SEDs consist of the AKARI 9 μm , 18 μm , the WISE 22 μm , the Herschel 70 μm , 160 μm , 250 μm , 350 μm and 500 μm data points. The thick solid line shows the best-fit model, while the dotted, thin solid, dashed and dash-dotted lines correspond to the PAH, hot, warm and cold dust components, respectively.

Table 1. Observation data properties

Satellite	Center wavelength	Pixel scale	FWHM of PSF
AKARI*	9 μm		5".5
	18 μm	4".68	5".7
	70 μm	3".2	6".0
Herschel†	160 μm	4".5	12".0
	250 μm	6".0	18".0
	350 μm	8".0	24".0
	500 μm	11".5	35".0
WISE‡	22 μm	1".375	12".0

* Onaka et al. (2007)

† Molinari et al. (2016)

‡ Cutri et al. (2013)

(Hi-GAL DR1 images: covering $-70^\circ \lesssim l \lesssim 68^\circ$, $|b| \leq 1^\circ$), which had been better calibrated with the ROMAGAL pipeline, were also released on the online site of the VIALACTEA project² (Molinari et al. 2016). Moreover, we used the WISE 22 μm band images to investigate the distribution of a hot dust (~ 120 K) component. The AllWISE data had been improved with enhanced sensitivity and accuracy compared with earlier WISE data releases (Cutri et al. 2013). The WISE data are given in units of DN, and the DN-to-Jy conversion factor is 5.2269×10^{-5} (Cutri et al. 2013; http://wise2.ipac.caltech.edu/docs/release/allwise/expsup/sec4_3a.html). The specifications of the observation data, i.e., the central

² VIALACTEA project <http://vialactea.iaps.inaf.it>

wavelengths, the pixel scales and the sizes of the point spread functions (PSFs) are summarized in table 1.

In this study, we investigate the IR bubbles having the Herschel Hi-GAL data ($|b| \leq 1^\circ$) and known distances out of the IR bubbles studied by Hanaoka et al. (2019). 165 IR bubbles remain as our sample, which consist of 29 IR bubbles found by Hanaoka et al. (2019) and 136 IR bubbles studied by Hattori et al. (2016) (i.e., cataloged by Churchwell et al. 2006, 2007).

To investigate the spatial distributions of the dust components around the IR bubbles, model fittings are performed to local spectral energy distributions (SEDs) on a pixel-by-pixel basis for the $4R \times 4R$ region of each IR bubble, where R is the radius of the IR bubble. We smoothed and re-gridded all the images with the PSF size and the pixel size of the Herschel 500 μm band images, 35".0 and 11".5 \times 11".5, respectively. Background intensity levels are estimated by averaging the values of the pixels within the background regions defined by the same procedure as Hattori et al. (2016) and Hanaoka et al. (2019). The error of the intensity in each pixel is calculated from the standard deviation of the intensities within the background region and the systematic errors of 10% are also considered in the local SEDs for AKARI, WISE mid-IR and Herschel data (D. Ishihara et al. in preparation; Jarrett et al. 2011; Molinari et al. 2016). We created the local SED of each pixel and fitted it with a dust model which includes PAHs,

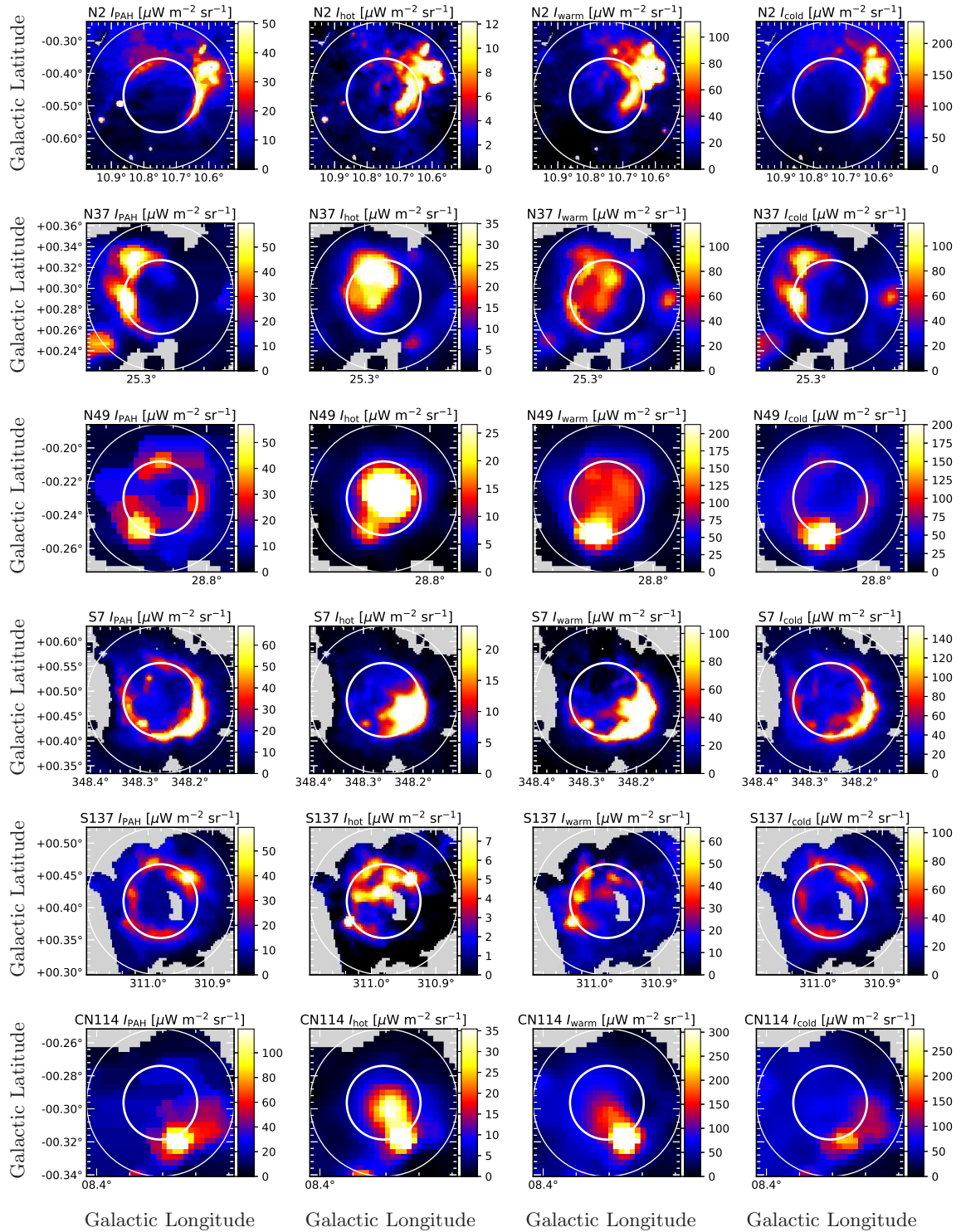


Fig. 2. Examples of the spatial distributions of the PAH, hot dust, warm dust and cold dust from left to right. The thick and thin white circles correspond to the R and $2R$ circular regions, respectively.

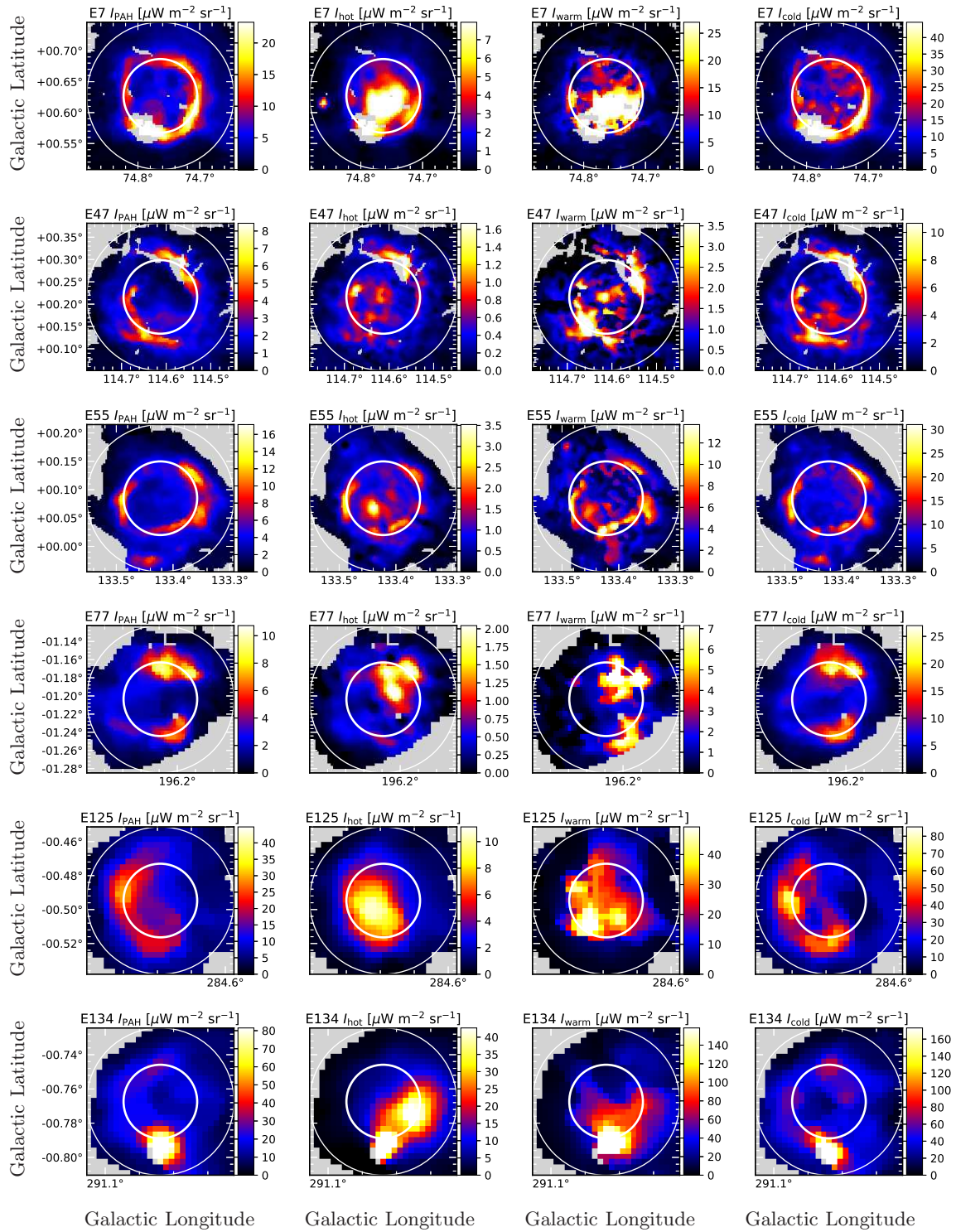


Fig. 2. Continued.

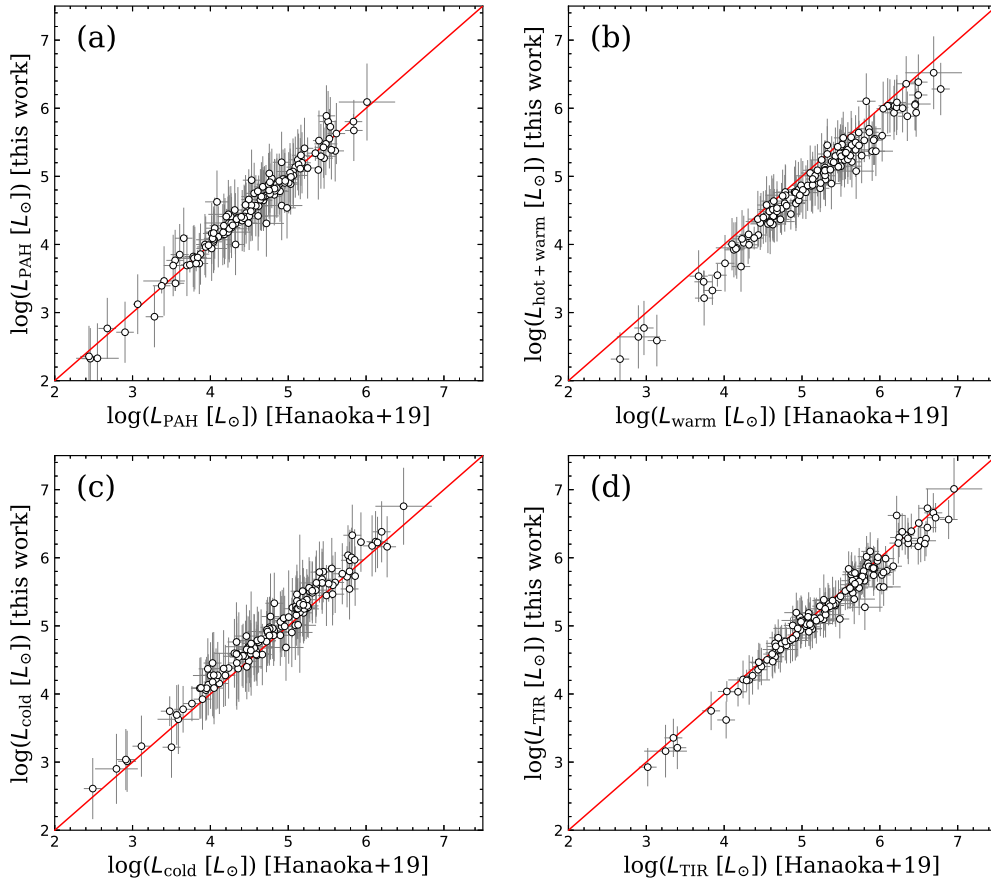


Fig. 3. Comparison between the results of the local SED fitting and those of Hanaoka et al. (2019). Each panel shows the comparison of (a) PAH luminosity, (b) hot and warm dust luminosity, (c) cold dust luminosity and (d) total IR luminosity, respectively. The red lines in each panel correspond to $y = x$.

hot dust, warm dust and cold dust components as follows:

$$F_{\nu}(\lambda) = aI_{\nu, \text{PAH}}(\lambda) + b\lambda^{-\beta_{\text{h}}} B_{\nu}(\lambda, T_{\text{h}}) + c\lambda^{-\beta_{\text{w}}} B_{\nu}(\lambda, T_{\text{w}}) + d\lambda^{-\beta_{\text{c}}} B_{\nu}(\lambda, T_{\text{c}}), \quad (1)$$

where $I_{\nu, \text{PAH}}(\lambda)$ is a PAH intensity model as a function of λ (Draine & Li 2007), $B_{\nu}(\lambda, T)$ is the Planck function with dust temperature T , and β is the emissivity power-law index. The temperatures of the warm and cold dust components are allowed to vary around ~ 60 K and ~ 20 K, respectively, as the initial parameters estimated from the SEDs of each IR bubble in Hanaoka et al. (2019). While that of the hot dust component is fixed at 123 K which is a typical value of the IR bubbles analyzed in this study. The emissivity power-law index generally shows a value near 2 for H II regions in our Galaxy (Anderson et al. 2012; Hanaoka et al. 2019), however, it can vary depending on the optical properties of dust grains. Here, the emissivity power-law index of the cold dust component, β_{c} , is set to be free, when the β_{c} value of 2 is not statistically acceptable in the SED fitting.

Figure 1 shows examples of the local SED-fitting results

for S7 (named ‘‘RCW 120’’ by Rodgers et al. 1960). The pixel denoted with ‘‘A’’ in the left panel of figure 1 is dominated by the hot dust component, while the pixel denoted with ‘‘B’’ requires the emissivity power-law index higher than 2. When the SED fitting is statistically rejected, a not a number (i.e., NaN) is assigned to the corresponding pixel (i.e., masked). To remove outliers, we applied a median filter, replacing a central pixel with the median value of the surrounding 3×3 pixels. If the masked region occupies more than 50% of the entire area within $2R$, we removed the corresponding IR bubbles from our sample. As a result, we obtain the brightness distributions of 157 IR bubbles, which is 95% of the 165 IR bubbles. Examples of the brightness distributions thus obtained are shown in figure 2.

In order to check the consistency between the results of Hanaoka et al. (2019) and local SED fitting results in this study, the IR luminosities integrated over the area of $< 2R$ are calculated for all the components, based on the brightness distributions derived with the local SED fitting. Figure 3 shows comparison between the luminosities thus

obtained from the local SED fitting and the luminosities estimated from the photometry fluxes within the $2R$ circular regions in Hanaoka et al. (2019). Here, we compare the warm dust luminosities of Hanaoka et al. (2019) with the sum of the hot and warm dust luminosities of the local SED fitting. Figure 3 shows an overall consistency between the results of Hanaoka et al. (2019) and the local SED fitting.

3 Result

To estimate the positions of the heating sources, we investigate the brightness ratio maps of $I_{\text{hot}}/I_{\text{TIR}}$ for the IR bubbles. Figure 4 shows the $I_{\text{hot}}/I_{\text{TIR}}$ maps for the sample IR bubbles in figure 2. The previous study by Hattori et al. (2016) showed that the color temperature of the dust emission peaks near the bubble centers for many of the well-defined closed bubbles, indicating the presence of heating sources (i.e., massive ionizing stars) in the centers. In our study, we choose only the IR bubbles which have a clear single $I_{\text{hot}}/I_{\text{TIR}}$ peak, so that we can mitigate the effect of mistakenly selecting a hot spot irrelevant to a massive star or confusion sources. Then we hereafter regard the positions of the $I_{\text{hot}}/I_{\text{TIR}}$ peaks as those of the heating sources. We obtain the peak position of $I_{\text{hot}}/I_{\text{TIR}}$ within the inner edge of the shell (defined as $0.8R$) for each IR bubble. When there is no significant hot dust emission detected within the shell boundary, we obtain the peak position of the warm dust component, using the $I_{\text{warm}}/I_{\text{TIR}}$ map instead of the $I_{\text{hot}}/I_{\text{TIR}}$ map. We then derive the peak positions for 117 IR bubbles, which have a single peak clearly identified within the shell boundary, out of the 165 IR bubbles (their peak positions are summarized in Appendix). For 7 out of the 117 IR bubbles, we used the $I_{\text{warm}}/I_{\text{TIR}}$ maps to investigate the peak positions. Then, we define the offset value from the center of each shell as the distance between the shell center and the peak position, R_{pp} , relative to the angular shell radius R (see the upper panel of figure 5). The lower panel of figure 5 shows the resultant R_{pp}/R plotted against the Galactocentric distance. The values of R and the Galactocentric distance of each IR bubble are cataloged in Hanaoka et al. (2019). The error of R_{pp} is evaluated by a quarter of the PSF size ($35''.0$) of the Herschel 500 μm band images (i.e., $9''$, similar to the pixel scale of $11''.5$). From this panel, we find that many IR bubbles in inner Galactic regions tend to have large offsets from the centers of the PDR shells; with the Poisson statistics, $29 \pm 6\%$ (28/96) of the IR bubbles at < 8 kpc have $R_{\text{pp}}/R > 0.6$, while $14 \pm 8\%$ (3/22) of the IR bubbles at > 8 kpc have $R_{\text{pp}}/R > 0.6$, and thus the difference is marginally significant, although the statistics are not good enough for the latter.

Figure 6 shows the brightness ratio maps of $I_{\text{PAH}}/I_{\text{TIR}}$ for the sample IR bubbles in figure 2. From the $I_{\text{PAH}}/I_{\text{TIR}}$ distribution maps, we investigate the radial profiles of $I_{\text{PAH}}/I_{\text{TIR}}$ averaged over the pixels within a certain radial position r , which are derived by systematically reducing the resolution of $I_{\text{PAH}}/I_{\text{TIR}}$ maps to match the lowest resolution in our sample. Figure 7 shows the $I_{\text{PAH}}/I_{\text{TIR}}$ radial profiles plotted against r/R , color-coded according to the Galactocentric distance. This result shows that $I_{\text{PAH}}/I_{\text{TIR}}$ monotonically increases with r to $\sim R$ which is the radius of each PDR shell. This global trend is reasonable because the PAH emission dominates in the PDR shells as pointed out by Hattori et al. (2016). Figure 7 also shows that $I_{\text{PAH}}/I_{\text{TIR}}$ systematically increases with the Galactocentric distance, while the radial profiles are similar among those at different Galactocentric distances, as seen in the right panel of the figure. This is consistent with the result of $L_{\text{PAH}}/L_{\text{TIR}}$ shown in Hanaoka et al. (2019), further indicating that IR bubbles in outer Galactic regions have systematically (i.e., not locally but globally) high $L_{\text{PAH}}/L_{\text{TIR}}$ within their $2R$ regions.

We quantify the local spatial variation of the PAH intensity within each IR bubble. To remove the radial global trend of the PAH intensity as seen in figure 7, we normalize the $I_{\text{PAH}}/I_{\text{TIR}}$ maps with the radial profile of each IR bubble (i.e., setting the azimuthally-averaged value to be a unity for given r). Figure 8 shows the resultant $I_{\text{PAH}}/I_{\text{TIR}}$ maps after removal of the radial trend for the same IR bubbles as in figure 6. We obtain the coefficients of variations (CVs) of the $I_{\text{PAH}}/I_{\text{TIR}}$ values within the $2R$ circular region in each IR bubble, which are calculated as the standard deviations divided by the mean values. We compare the $I_{\text{PAH}}/I_{\text{TIR}}$ CVs of the IR bubbles in inner Galactic regions with those in outer Galactic regions.

Figure 9 shows that the IR bubbles in inner Galactic regions are likely to have higher $I_{\text{PAH}}/I_{\text{TIR}}$ CVs than the IR bubbles in outer Galactic regions, indicating that $I_{\text{PAH}}/I_{\text{TIR}}$ in inner Galactic regions have not only higher values on average but also larger spatial variations relative to the average than those in outer Galactic regions.

In fitting the SEDs, some IR bubbles show the pixels where β_c of 2 is not statistically acceptable. To reliably identify the pixels having $\beta_c \neq 2$, we selected the pixels whose β_c values are different from 2 with 5σ significance. For the IR bubble where such pixels occupy 20% of the total pixels within the $2R$ circular region, the averaged β_c in the $2R$ region is plotted against the Galactocentric distance with the standard deviation as an error bar in figure 10. This figure shows that β_c is equal to 2 within the error bars for almost all the IR bubbles, which is consistent with the fitting results of the SEDs created from the pho-

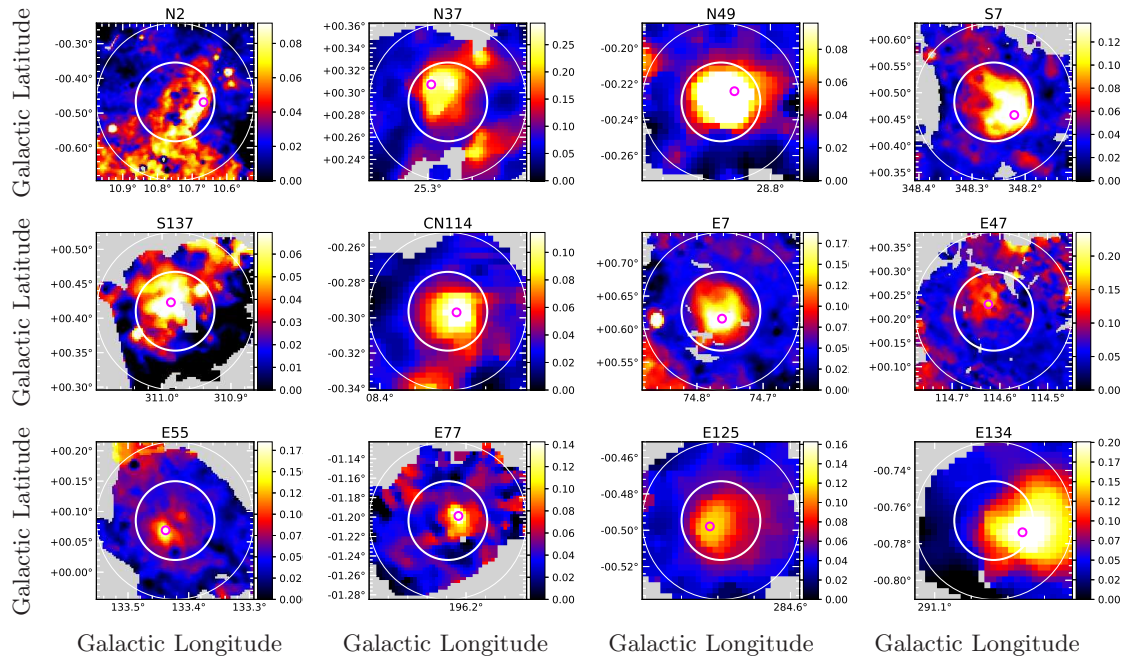


Fig. 4. Examples of the $I_{\text{hot}}/I_{\text{TIR}}$ maps, together with the peak positions of the hot dust emission denoted with magenta circles. The thick and thin white circles correspond to the R and $2R$ circular regions, respectively.

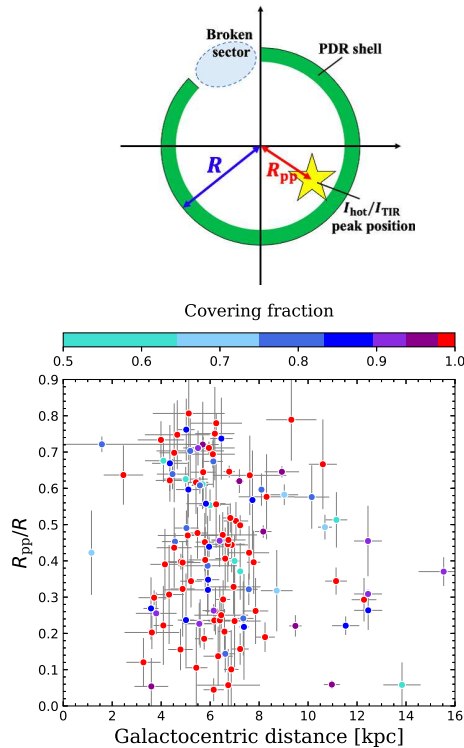


Fig. 5. (Upper) schematic view to explain the definition of R_{pp} . (Lower) the peak position of the hot dust emission relative to the IR bubble radius, R_{pp}/R , plotted as a function of the Galactocentric distance. The data points are color-coded according to the CF obtained in Hanaoka et al. (2019) (the color will be discussed in Section 4).

tometry fluxes integrated within the $2R$ circular regions in Hanaoka et al. (2019) where $\beta_c = 2$ is acceptable for all the IR bubbles. The averaged value decreases with the Galactocentric distance; the β_c values tend to be higher than 2 in inner Galactic regions, while they are lower than 2 in outer Galactic regions. A Kolmogorov-Smirnov (K-S) test shows that the difference is statistically significant (p-value is 0.01), although the uncertainties of β_c are large. Such a decreasing trend of β_c is observed in nearby galaxies as well, e.g., M31 and M33 (Smith et al. 2012; Draine et al. 2014; Tabatabaei et al. 2014). These previous studies of the nearby galaxies suggest a change in the dust properties at 3–4 kpc from the Galactic center based on the change of the β_c value. The result of figure 10 shows that the transition point of our Galaxy is located around ~ 8 kpc from the Galactic center. Also, Giannetti et al. (2017) show that the gas-to-dust ratio in our Galaxy increases with the Galactocentric distance while the metallicity decreases from IR and CO observations.

4 Discussion

4.1 Variations of the IR bubble properties along the whole Galactic plane

We examine the relation between the positions of the heating sources and the shell morphology. We show that many IR bubbles in inner Galactic regions have large R_{pp}/R , which indicates that the heating sources are likely to be

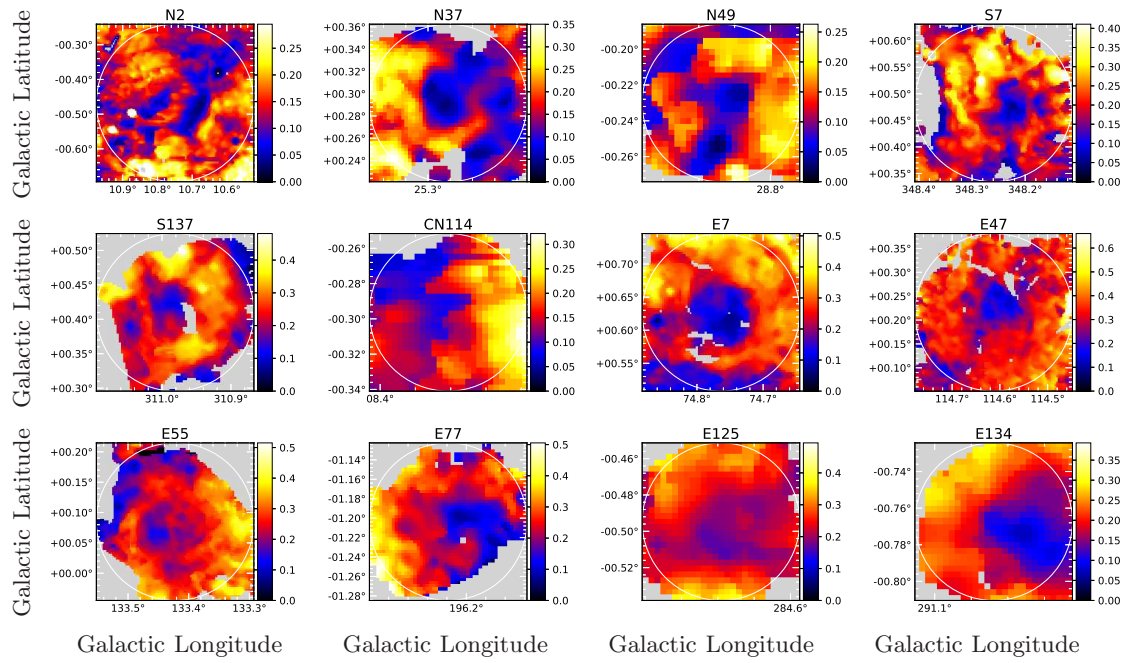


Fig. 6. Examples of the $I_{\text{PAH}}/I_{\text{TIR}}$ maps. The white circles correspond to the $2R$ circular regions.

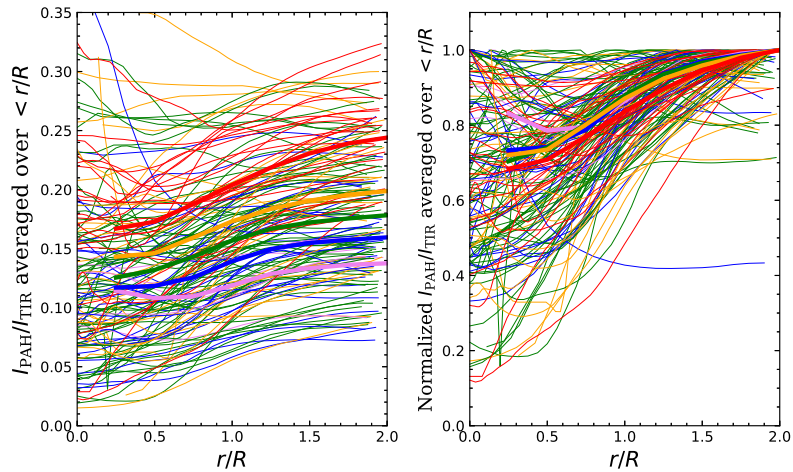


Fig. 7. (Left) radial profiles of $I_{\text{PAH}}/I_{\text{TIR}}$ averaged over the pixels within a circular region of a radius r . (Right) the same as the left panel, but all the profiles are normalized. The profiles are color-coded with the Galactocentric distance; the violet, blue, green, orange and red curves correspond to 0–3, 3–5, 5–7, 7–9 and 9–12 kpc from the Galactic center, respectively, while the bold curves are their averages.

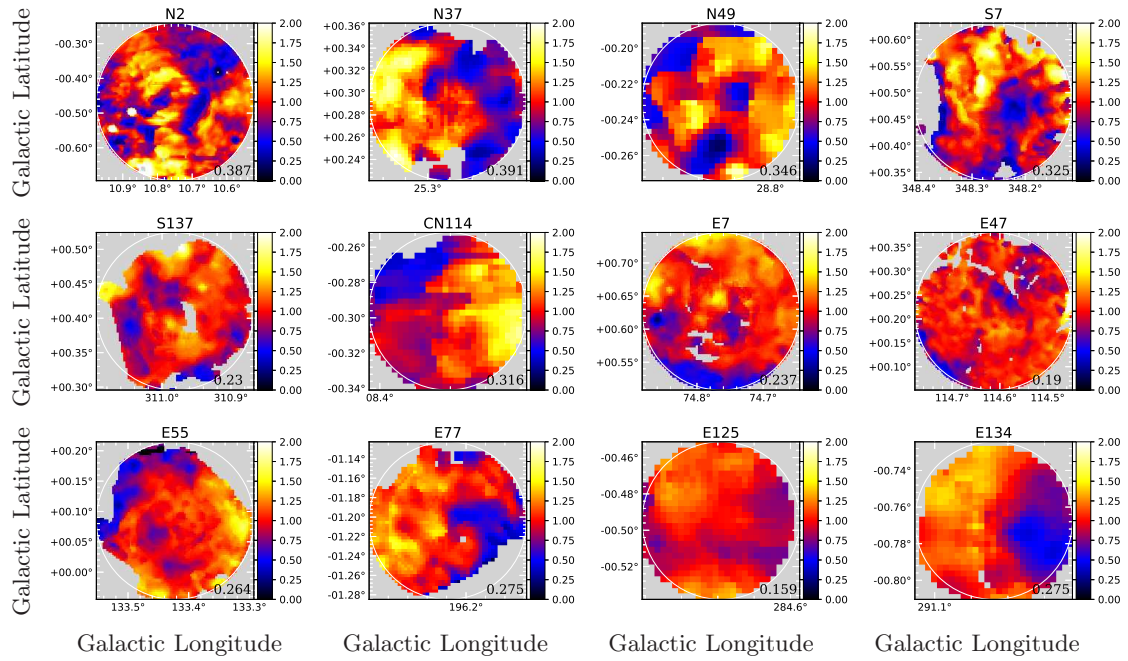


Fig. 8. Examples of the $I_{\text{PAH}}/I_{\text{TIR}}$ maps after removing the radial trends of the PAH emission with the radial profiles (see figure 7). The white circles correspond to the $2R$ circular regions. The coefficients of variations (CVs) of the $I_{\text{PAH}}/I_{\text{TIR}}$ are denoted at the right bottom of each panel.

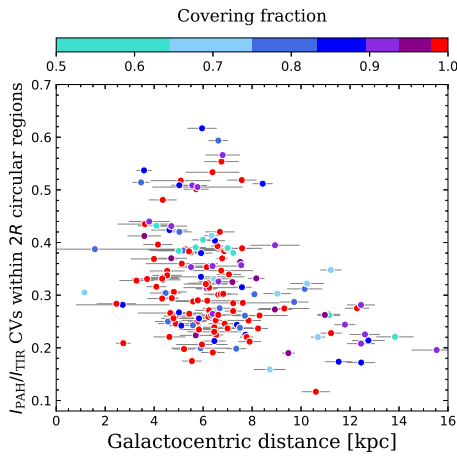


Fig. 9. Coefficients of variations (CVs), calculated as the standard deviations divided by the mean values, within the $2R$ circular regions of the $I_{\text{PAH}}/I_{\text{TIR}}$ maps after removing the radial profile (figure 7), plotted against the Galactocentric distance. The data points are color-coded according to the CF obtained in Hanaoka et al. (2019) (the color will be discussed in Section 4).

closer to the dense shell regions around the IR bubbles. For example, for the IR bubbles with offsets as large as $R_{\text{pp}}/R > 0.6$, 28 ± 5 and 3 ± 2 IR bubbles are located at < 8 kpc and > 8 kpc, respectively, with the errors from the Poisson statistics. In figure 5, to show the dependence of the offsets on the covering fractions of the PAH shells (CFs) obtained by Hanaoka et al. (2019), we further color-coded the data points with CF. The figure suggests that

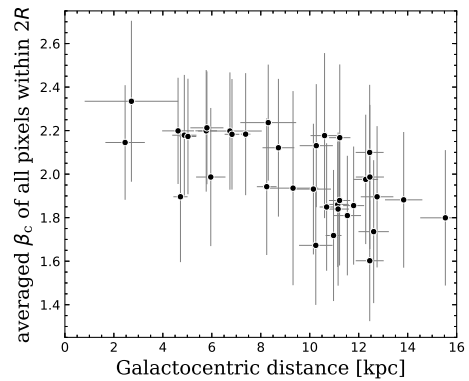


Fig. 10. Averaged emissivity power-law index of the cold dust component, β_c , within the $2R$ circular region for each of the IR bubbles where 20% of the total pixels within the $2R$ region are unacceptable for $\beta_c = 2$. The error bars correspond to the standard deviations of the β_c values in the $2R$ regions.

the fraction of closed bubbles may increase at low R_{pp}/R . For example, the IR bubbles with CF=1.0 occupy $70 \pm 20\%$ of the total IR bubbles at $R_{\text{pp}}/R < 0.2$, while they are $52 \pm 7\%$ at $R_{\text{pp}}/R > 0.2$.

Then, for the broken bubbles, we obtained the direction of the broken sector for each IR bubble based on the CF estimation in Hanaoka et al. (2019). We investigate the difference in the direction angle, $\theta_{\text{BS-pp}}$, between the heating source position and the broken sector direction as viewed

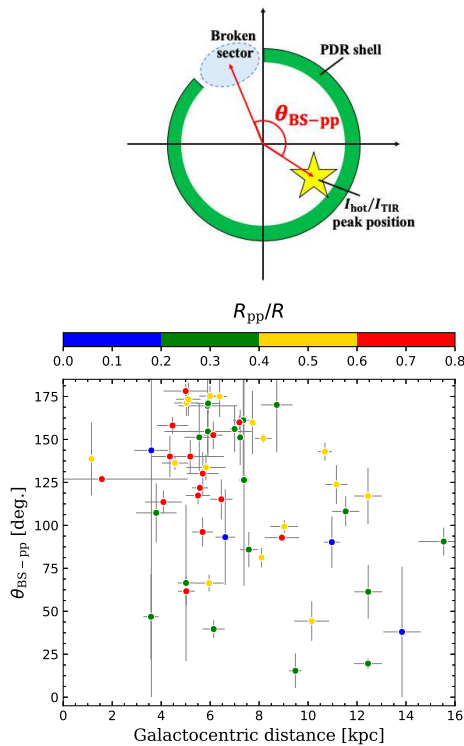


Fig. 11. (Upper) schematic view to explain the definition of θ_{BS-pp} . (Lower) the angle between the positions of the peak and the broken sector, θ_{BS-pp} , plotted as a function of the Galactocentric distance. The data points are color-coded according to R_{pp}/R .

from the shell center (see the upper panel of figure 11). As errors of θ_{BS-pp} , we consider those associated with the positional uncertainties of the heating sources which are evaluated to be one image pixel. Then we calculate the angle which are subtended by the chord of one pixel length at R_{pp} from the center. The relation thus obtained is shown in the lower panel of figure 11, from which we find that the heating sources are located nearly on the opposite side of the broken sector directions (i.e., $\theta_{BS-pp} \sim 180^\circ$) for a significant fraction of the IR bubbles in inner Galactic regions. In the figure, the color is added to the data points to show R_{pp}/R , where it is found that the IR bubbles with large R_{pp}/R tend to have large θ_{BS-pp} . Hence a significant fraction of the IR bubbles in inner Galactic regions have heating sources largely offset from the center to the shell, where the broken sector directions are related to the positions of the heating sources nearly on their opposite sides.

One possible reason for the large offset of the heating sources and the large θ_{BS-pp} value in inner Galactic regions is local density gradients within each IR bubble, i.e., H II regions may be easier to expand toward the lower density direction, and the lower density side of the shell tends

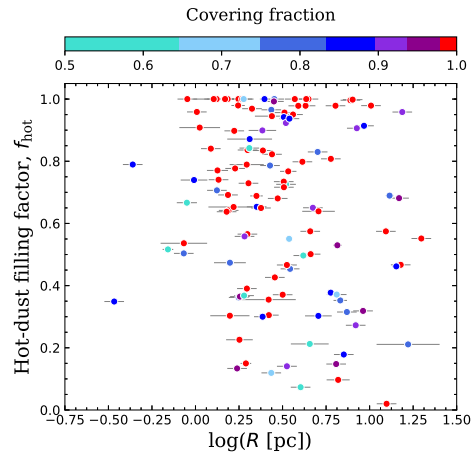


Fig. 12. Relation between the hot-dust filling factor in the H II regions and the shell radius of each IR bubble, color-coded according to the CF. The shell radii and CFs were obtained in Hanaoka et al. (2019).

to be broken. On the other hand, Hattori et al. (2016) mentioned that the offset of the heating sources can be explained by formation of massive stars on the boundary of the collided clouds, and in that case, the broken structure can be favorably observed. If the CCC process is important for the broken bubbles in inner Galactic regions, it is expected that their massive stars are substantially offset to the opposite side of the broken sector direction. This interpretation is also consistent with the result shown in the lower panel of figure 11, in which the IR bubbles with larger θ_{BS-pp} ($\sim 180^\circ$) tend to have larger offsets from the center.

To further discuss the morphology formation mechanisms of the IR bubbles, we investigate the hot-dust filling factor (f_{hot}) in the H II region of each IR bubble. We derive ratios of the pixels brighter than 20% of the I_{hot} intensity at the peak position of I_{hot}/I_{TIR} within the inner edge of the shell (i.e., $< 0.8R$). For the IR bubbles without significant hot dust emission within the shell boundaries, we used the I_{warm} intensity maps. Figure 12 shows f_{hot} plotted against the shell radius, color-coded according to CF. This figure shows that the large broken bubbles (i.e., $\log(R$ [pc]) > 0.6 and $CF < 0.9$ from Hanaoka et al. 2019) tend to have lower f_{hot} . Indeed, a K-S test shows that the distributions of the large broken bubbles and large closed bubbles (i.e., $\log(R$ [pc]) > 0.6 and $CF = 1.0$ from Hanaoka et al. 2019) are statistically different from each other (p-value is 0.009). Moreover, table 2 shows that 5 out of 10 large broken bubbles having f_{hot} lower than 0.5 also have $R_{pp}/R > 0.5$ and $\theta_{BS-pp} > 90^\circ$. Hattori et al. (2016) suggested that many of the large broken bubbles may have been formed through the CCC process. In this case, the H II gas and the hot dust are expected to be rather local-

Table 2. IR properties of the large broken bubbles having low f_{hot} .

	$\log(R [\text{pc}])^*$	f_{hot}	R_{pp}/R	$\theta_{\text{BS-PP}}$
N2	1.22 ± 0.18	0.21	0.72 ± 0.02	$127^\circ.0$
N6	0.87 ± 0.06	0.32	0.45 ± 0.02	$136^\circ.0$
N39	0.62 ± 0.06	0.50	0.68 ± 0.06	$114^\circ.0$
S1	0.66 ± 0.11	0.21	0.62 ± 0.03	$178^\circ.0$
S27	0.78 ± 0.01	0.38	0.76 ± 0.09	$62^\circ.0$
S66	0.83 ± 0.04	0.35	0.61 ± 0.02	$122^\circ.0$
S76	0.71 ± 0.08	0.30	0.44 ± 0.03	$66^\circ.0$
S92	1.15 ± 0.02	0.46	0.35 ± 0.03	$171^\circ.0$
E21	0.81 ± 0.06	0.37	0.58 ± 0.03	$99^\circ.0$
E95	0.85 ± 0.06	0.18	0.22 ± 0.03	$108^\circ.0$

* Hanaoka et al. 2019

ized on the dense shell formed through CCC than fill the inside of the shell. The above 5 large broken bubbles in the table may be candidate targets which have been formed by CCC.

In figure 9, to show the dependence of the CVs of $I_{\text{PAH}}/I_{\text{TIR}}$ on CFs, we color-coded the data points with CF. The figure shows that, for the IR bubbles in inner Galactic regions (< 8 kpc), 17 out of 25 bubbles which have the $I_{\text{PAH}}/I_{\text{TIR}}$ CVs larger than 0.4 are observed as broken bubbles, while 38 out of 102 bubbles with the $I_{\text{PAH}}/I_{\text{TIR}}$ CVs smaller than 0.4 are broken bubbles. The former ratio ($70 \pm 20\%$) is significantly higher than the latter ratio ($37 \pm 6\%$), based on the Poisson statistics. Hence, the broken morphology may be the key to understanding the large spatial variations of the fractional PAH intensities. We discuss possible processes to produce the observed large $I_{\text{PAH}}/I_{\text{TIR}}$ CVs in inner Galactic regions as seen in figure 9. Considering the possibility of PAH destruction around the IR bubbles, PAHs can be destroyed by UV radiation, hot gas and interstellar shocks (e.g., Tielens 2005; Rapacioli et al. 2005; Micelotta et al. 2010a, 2010b). First, we only discuss the effects of interstellar shocks, because the effects of the PAH destruction by the UV radiation and hot gas in H II regions are likely to be reflected by the $I_{\text{PAH}}/I_{\text{TIR}}$ radial profiles (figure 7), which are already removed from the $I_{\text{PAH}}/I_{\text{TIR}}$ distribution maps in deriving the CVs (figure 9). The PAH destruction in the interstellar shocks needs a shock velocity above 100 km s^{-1} (Micelotta et al. 2010a). The observed collisional velocities of CCC are as slow as $10\text{--}30 \text{ km s}^{-1}$ (e.g., Inoue & Fukui 2013; Fukui et al. 2016), which are too slow to destroy the PAHs.

Then, we discuss the possibility of PAH production around the IR bubbles. PAHs can be produced by shattering carbonaceous dust grains with the collisional velocity of about $1\text{--}100 \text{ km s}^{-1}$ (Jones et al. 1996); the collisional ve-

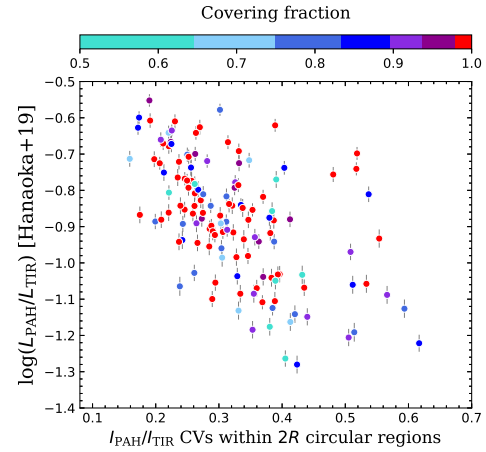


Fig. 13. Relation between $L_{\text{PAH}}/L_{\text{TIR}}$ obtained by Hanaoka et al. (2019) and the $I_{\text{PAH}}/I_{\text{TIR}}$ CVs, color-coded with the CF.

locities of CCC are in this velocity range. However, shortly after the production, PAHs might be destroyed by intense UV radiation from massive stars. We calculate the PAH destruction timescale in H II regions using a C-H band photo-dissociation time scale in the diffuse ISM, $\tau_{\text{UV,pd}}$, as described by the following equation (Jones et al. 2014; Jones & Habart 2015):

$$\tau_{\text{UV,pd}} = \frac{10^4}{G_0} \left\{ 2.7 + \frac{6.5}{(a[\text{nm}])^{1.4}} + 0.04(a[\text{nm}])^{1.3} \right\} \text{ [yr]}, \quad (2)$$

where G_0 and a are the radiation field intensity integrated for far-UV wavelengths relative to the solar neighborhood and grain radius, respectively. We adopted the typical G_0 of $10^2\text{--}10^4$ in H II regions whose bolometric luminosities of sources are in a range of $10^3\text{--}10^5 L_\odot$ (Decataldo et al. 2017) and the typical PAH size of 6 \AA (Tielens 2005) to find that $\tau_{\text{UV,pd}} \sim 10\text{--}10^3 \text{ yr}$. This calculation implies that PAHs produced through shattering of carbonaceous grains will be destroyed in the H II region within timescales much shorter than the lifetime of IR bubbles ($\sim 10^6 \text{ yr}$). Therefore, we can expect that CCC could decrease fractional PAH luminosities, $L_{\text{PAH}}/L_{\text{TIR}}$, as a whole with a large $I_{\text{PAH}}/I_{\text{TIR}}$ CV. Figure 13 indeed shows that the IR bubbles with low $L_{\text{PAH}}/L_{\text{TIR}}$ tend to have large $I_{\text{PAH}}/I_{\text{TIR}}$ CVs. Moreover, such IR bubbles tend to have lower CFs, which is in line with the CCC trend pointed out by Hattori et al. (2016). Hence, the large spatial variations of $I_{\text{PAH}}/I_{\text{TIR}}$ may also be caused by the CCC process.

We discuss the β_c values in the context of the properties of the interstellar dust. According to the standard dust model defined in Desert, Boulanger and Puget (1990), $\beta_c \simeq 2$ is expected for silicate grains, while $\beta_c \simeq 1$ for carbonaceous grains. Indeed, Mennella et al. (1998) obtained that amorphous carbon grains have a β_c value of ~ 1 which

is lower value than that of amorphous silicate grains in their laboratory measurement. Among them, carbon-rich (C-rich) asymptotic giant branch (AGB) stars are considered as suppliers of carbonaceous dust including PAHs, while oxygen-rich (O-rich) AGB stars as suppliers of silicate dust (Latter 1991; Tielens 2008). Ishihara et al. (2011) investigated the distributions of C-rich and O-rich AGB stars in our Galaxy and obtained that the C-rich AGB stars are uniformly distributed within the Galactic disk, while the O-rich AGB stars are concentrated toward the Galactic center. Moreover, the result of $L_{\text{PAH}}/L_{\text{TIR}}$ of Hanaoka et al. (2019) suggests that the environments in outer Galactic regions belong to those relatively rich in PAHs. The result shows the tendency that $\beta_c \gtrsim 2$ for inner Galactic regions while $\beta_c \lesssim 2$ for outer Galactic regions. Thus, the trend of the β_c value also supports that the IR bubbles are relatively rich in carbonaceous dust in outer Galactic regions.

4.2 Properties of the IR bubbles in the cloud collision environments

To verify the IR properties in the cloud collision environments, we examine the spatial distributions of the dust components for the IR bubbles which are studied well with CO and most probably associated with CCC. Among our sample IR bubbles, there are 6 IR bubbles having bridge features in the CO position-velocity maps within the $2R$ regions, which suggest that the cloud collisions are still ongoing around the IR bubbles (N18; Torii et al. 2018a, N35; Torii et al. 2018b, N37; Baug et al. 2016, N49; Dewangan et al. 2017, S7; Torii et al. 2015, S44; Kohno et al. 2018). In table 3, we summarize the properties of those IR bubbles obtained by the local SED fittings. Two of them (N37 and S7) have the CCC trends in the IR properties, i.e., $R_{\text{pp}}/R > 0.5$, $\theta_{\text{BS-pp}} > 90^\circ$ and $I_{\text{PAH}}/I_{\text{TIR}} \text{ CV} > 0.3$. However, the other IR bubbles have small R_{pp}/R and closed shells (see table 3 and left panels in figure 14). We interpret that the latter are formed by nearly head-on collisions between two clouds and viewed face-on from us. In this case, the massive star is presumably located near the shell center and the shell morphology is likely to appear ‘‘closed’’.

The center panels in figure 14 show the $I_{\text{PAH}}/I_{\text{TIR}}$ distribution maps. Indeed, N37 and S7, which have the CCC trends in the IR properties, have clearly high $I_{\text{PAH}}/I_{\text{TIR}}$ values in the white square regions, where the cloud collisions are likely to be underway, judging from the positional coincidence with the bridge features in the CO position-velocity maps. Those trends are consistent with our hypothesis, i.e., the CCC process can produce PAHs through

Table 3. IR properties of the IR bubbles having bridge features in the CO position-velocity maps.

	CF*	R_{pp}/R	$\theta_{\text{BS-pp}}$	$I_{\text{PAH}}/I_{\text{TIR}}$ CV
N18	1.00	0.40 ± 0.02	–	0.31
N35	1.00	0.20 ± 0.05	–	0.43
N37	0.67	0.61 ± 0.07	$96^\circ.0$	0.39
N49	1.00	0.44 ± 0.11	–	0.35
S7	0.96	0.62 ± 0.03	$160^\circ.0$	0.33
S44	1.00	0.16 ± 0.06	–	0.26

* Hanaoka et al. 2019

shattering of carbonaceous dust as discussed above. On the other hand, the maps of N18, N35, N49 and S44 show that the $I_{\text{PAH}}/I_{\text{TIR}}$ values are not systematically higher in the square regions. The effects of the PAH production process on the $I_{\text{PAH}}/I_{\text{TIR}}$ value might be difficult to be observed due to the overlap of multiple components along the line of sight, when CCC is viewed face-on from us.

The right panels in figure 14 show that there are some clumps having $\beta_c > 2.0$ within the $2R$ regions. N37 and S7 have large β_c in the white square regions where the bridge features have been observed. Such high β_c values have been observed in dense cold molecular clouds (e.g., Kuan et al. 1996; Lis & Menten 1998; Planck Collaboration et al. 2011), and dust grains coated with thick icy mantles can have β_c significantly higher than 2 (e.g., Aannestad 1975; Güttler 1952; Wickramasinghe 1967). Therefore, this result suggests that CCC may increase β_c due to the presence of cold dense clouds which are likely to be formed on the collision surface. The coagulation on dust grains requires gas densities of $n_{\text{H}} > 10^4 \text{ cm}^{-3}$ (Chokshi et al. 1993), thus the high β_c regions are likely candidates for massive star formation. To verify the hypothesis, we plot massive clumps identified by Csengeri et al. (2014) with ATLASGAL surveys in the right panels of figure 14. The massive clumps are located near some of the high β_c regions (e.g., those in N37, N49 and S7), but not for the other high β_c regions, which do not provide us with a very convincing result. Hence, high R_{pp}/R and $\theta_{\text{BS-pp}}$ as well as the local enhancements of the PAH fractional intensity ($I_{\text{PAH}}/I_{\text{TIR}} > 0.3$) and the cold dust emissivity power-law index ($\beta_c > 2$) may be good probes to search for nearly edge-on CCC candidates, while they may not be valid for face-on CCC. Whichever the case is, we need more statistics to verify the relationships between IR and radio CO properties for the IR bubbles indicative of CCC.

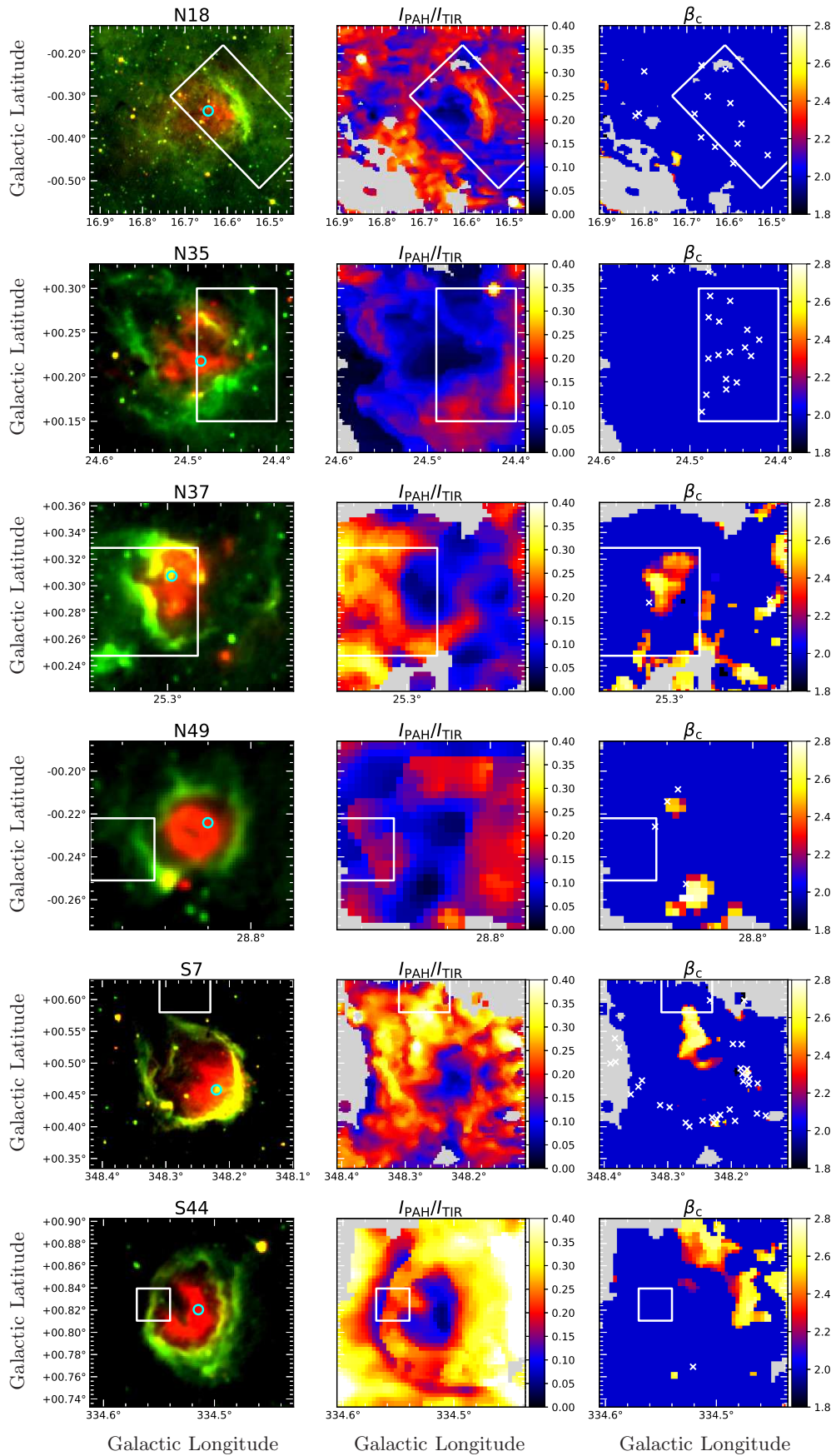


Fig. 14. PAH intensity ratio, $I_{\text{PAH}}/I_{\text{TIR}}$, and the emissivity power-law index of the cold dust component, β_c , maps of the IR bubbles having bridge features in the CO position-velocity maps. The left panels show the AKARI 9 μm and 18 μm band images in green and red, respectively. The cyan circles in the left panels correspond to the peak positions of the hot dust emissions. The white squares correspond to the regions where the bridge features had been observed (N18; Torii et al. 2018a, N35; Torii et al. 2018b, N37; Baug et al. 2016, N49; Dewangan et al. 2017, S7; Torii et al. 2015, S44; Kohno et al. 2018). The white crosses in the right panels correspond to the positions of massive clumps identified by Csengeri et al. (2014).

5 Summary

Using AKARI, Herschel and WISE data, we have studied the spatial distributions of dust components around 165 IR bubbles along the whole Galactic plane ($0^\circ \leq l < 360^\circ$, $|b| \leq 5^\circ$), which are decomposed into PAH, hot dust (123 K), warm dust (~ 60 K) and cold dust (~ 20 K). As a result, we find that the offsets of dust heating sources from the shell centers, which are estimated with the hot or warm dust emission, in inner Galactic regions are larger than those in outer Galactic regions. Moreover, the spatial variations of the $I_{\text{PAH}}/I_{\text{TIR}}$ and the β_c values around the IR bubbles in inner Galactic regions are larger than those in outer Galactic regions. The offsets of dust heating sources suggest that a local density gradient within each IR bubble or the CCC process may make larger contribution to forming the shell morphology in inner Galactic regions. Considering possible production and destruction processes of PAHs around the IR bubbles, we suggest that the large spatial variations of the PAH intensities in inner Galactic regions may be caused by CCC. The β_c trend suggests that the IR bubbles may be relatively rich in carbonaceous dust in outer Galactic regions, which is aligned with the result of the higher ratios of PAH to dust in Hanaoka et al. (2019). Finally, we discuss the IR properties of the cloud collision environments around the IR bubbles which are studied with the previous CO observations, and our results suggest the possibility that the dust properties are influenced by the cloud collision.

Acknowledgments

This research is based on observations with AKARI, a JAXA project with the participation of ESA. Herschel is an ESA space observatory with science instruments provided by European-led Principal Investigator consortia and with important participation from NASA. This publication makes use of data products from the Wide-field Infrared Survey Explorer, which is a joint project of the University of California, Los Angeles, and the Jet Propulsion Laboratory/California Institute of Technology, funded by the National Aeronautics and Space Administration. We thank all the members of the AKARI, Herschel, and WISE projects, particularly the all-sky survey, Hi-GAL, and AllWISE data reduction teams. This research was supported by JSPS KAKENHI Grant Number 18H01252.

Appendix. Summary of the IR properties derived in this study.

Table 4. Summary of the local SED properties.

Name	$l_{\text{pp}} [^\circ]$	$b_{\text{pp}} [^\circ]$	R_{pp}/R	$\theta_{\text{BS-pp}} [^\circ]$	f_{hot}	$I_{\text{PAH}}/I_{\text{TIR}}$	CV	β_c
N2	10.67	-0.47	0.72±0.02	127.0 ± 2.0	0.21	0.39	—	—
N4	11.90	0.74	0.34±0.07	—	0.57	0.20	—	—
N6	12.48	-0.61	0.45±0.02	136.0 ± 4.0	0.32	0.25	—	—
N10	13.18	0.04	0.39±0.10	—	0.84	0.40	—	—
N11	13.23	0.08	0.32±0.13	—	0.84	0.26	2.18±0.28	—
N12	13.77	-0.03	0.62±0.03	—	0.98	0.48	—	—
N14	—	—	—	—	—	0.17	—	—
N15	—	—	—	—	—	0.42	—	—
N16	15.00	0.05	0.32±0.06	155.0 ± 15.0	0.91	0.34	—	—
N18	16.65	-0.34	0.40±0.02	—	1.00	0.31	—	—
N29	23.06	0.55	0.29±0.05	—	1.00	0.22	—	—
N30	23.12	0.55	0.75±0.13	—	0.54	0.32	—	—
N34	—	—	—	—	—	0.39	—	—
N35	24.49	0.22	0.20±0.05	—	1.00	0.43	—	—
N36	24.84	0.09	0.26±0.06	107.0 ± 17.0	0.65	0.44	—	—
N37	25.30	0.31	0.61±0.07	96.0 ± 8.0	0.84	0.39	—	—
N39	25.36	-0.18	0.68±0.06	114.0 ± 7.0	0.50	0.43	—	—
N40	25.38	-0.36	0.81±0.13	—	1.00	0.36	—	—
N44	—	—	—	—	—	0.22	2.20±0.24	—
N45	26.98	-0.07	0.75±0.09	—	0.57	0.27	—	—
N46	27.32	-0.12	0.67±0.11	140.0 ± 12.0	0.65	0.33	—	—
N47	28.01	-0.02	0.73±0.05	—	0.81	0.37	—	—
N49	28.82	-0.22	0.44±0.11	—	0.97	0.35	—	—
N50	29.01	0.08	0.70±0.09	140.0 ± 10.0	0.83	0.39	—	—
N52	—	—	—	—	—	0.42	—	—
N54	31.14	0.29	0.67±0.07	153.0 ± 8.0	0.36	0.31	—	—
N56	32.59	0.00	0.47±0.12	—	0.96	0.52	—	—
N59	33.09	-0.12	0.40±0.02	—	0.57	0.25	—	—
N61	34.17	0.17	0.55±0.04	175.0 ± 6.0	0.73	0.41	—	—
N62	34.33	0.20	0.64±0.10	—	0.78	0.50	—	—
N64	34.76	-0.67	0.04±0.03	—	0.98	0.35	—	—
N65	35.01	0.33	0.26±0.07	—	0.73	0.26	—	—
N68	35.66	-0.04	0.24±0.03	—	0.47	0.29	—	—
N71	38.31	-0.03	0.26±0.02	40.0 ± 5.0	0.27	0.31	—	—
N72	38.35	-0.13	0.22±0.15	126.0 ± 62.0	0.79	0.24	2.18±0.28	—
N73	38.74	-0.14	0.39±0.14	170.0 ± 28.0	1.00	0.20	—	—
N74	38.91	-0.44	0.10±0.11	—	1.00	0.38	—	—
N77	40.43	-0.04	0.72±0.12	130.0 ± 12.0	0.36	0.22	—	—
N79	41.52	0.04	0.64±0.11	—	1.00	0.28	—	—
N80	—	—	—	—	—	0.36	—	—
N81	42.06	-0.59	0.71±0.02	—	0.55	0.21	—	—
N82	42.11	-0.63	0.40±0.09	—	0.83	0.26	2.21±0.26	—
N84	42.83	-0.15	0.57±0.14	160.0 ± 18.0	0.35	0.23	—	—
N90	43.77	0.07	0.41±0.09	—	0.69	0.30	—	—
N91	44.26	0.09	0.78±0.03	—	0.02	0.31	—	—
N92	44.34	-0.82	0.24±0.09	—	0.90	0.19	—	—
N95	45.39	-0.72	0.56±0.12	—	0.64	0.27	—	—
N98	47.03	0.23	0.14±0.08	—	0.65	0.26	—	—

Table 4. (Continued)

Name	l_{pp} [°]	b_{pp} [°]	R_{pp}/R	$\theta_{\text{BS-pp}}$ [°]	f_{hot}	$I_{\text{PAH}}/I_{\text{TIR}}$	CV	β_{c}
N101	—	—	—	—	—	0.33	—	—
N114	52.25	0.71	0.26±0.09	—	1.00	0.25	—	—
N115	53.55	−0.00	0.16±0.04	—	0.31	0.27	—	—
N117	54.10	−0.06	0.44±0.08	—	0.43	0.25	—	—
N120	—	—	—	—	—	0.52	—	—
N123	57.54	−0.28	0.58±0.12	—	0.37	0.26	2.24±0.27	—
N124	58.61	0.63	0.24±0.10	161.0 ± 34.0	0.71	0.20	—	—
N126	59.61	0.31	0.42±0.07	—	0.95	0.39	—	—
N127	60.66	−0.03	0.60±0.04	81.0 ± 6.0	0.50	0.30	—	—
N130	—	—	—	—	—	0.32	—	—
N131	—	—	—	—	—	0.40	—	—
N133	63.17	0.45	0.40±0.09	—	0.96	0.22	—	—
S1	349.81	−0.56	0.62±0.03	178.0 ± 4.0	0.21	0.38	—	—
S7	348.22	0.46	0.62±0.03	160.0 ± 4.0	0.13	0.33	—	—
S8	—	—	—	—	—	0.21	—	—
S11	345.49	0.40	0.20±0.06	—	0.74	0.39	—	—
S13	345.13	−0.75	0.65±0.02	—	0.50	0.37	—	—
S14	344.76	−0.54	0.18±0.03	—	0.80	0.25	—	—
S15	343.91	−0.65	0.23±0.07	—	0.79	0.29	—	—
S17	343.47	−0.04	0.45±0.08	—	1.00	0.29	—	—
S18	—	—	—	—	—	0.29	1.90±0.30	—
S20	—	—	—	—	—	0.36	—	—
S23	341.26	−0.35	0.48±0.07	—	0.39	0.38	—	—
S27	340.06	−0.14	0.76±0.09	62.0 ± 8.0	0.38	0.51	2.17±0.27	—
S29	338.91	0.62	0.23±0.06	151.0 ± 20.0	0.90	0.51	—	—
S36	337.94	−0.48	0.49±0.05	171.0 ± 7.0	0.45	0.42	—	—
S37	337.69	−0.35	0.10±0.11	—	1.00	0.27	—	—
S41	—	—	—	—	—	0.33	—	—
S44	334.51	0.82	0.16±0.06	—	0.77	0.26	—	—
S51	332.67	−0.63	0.62±0.09	—	1.00	0.38	—	—
S62	331.33	−0.34	0.60±0.08	173.0 ± 10.0	0.30	0.24	—	—
S64	331.04	−0.14	0.71±0.05	117.0 ± 5.0	0.14	0.35	—	—
S66	330.84	−0.39	0.61±0.02	122.0 ± 3.0	0.35	0.24	—	—
S70	329.27	0.11	0.24±0.13	66.0 ± 46.0	0.94	0.27	—	—
S71	327.99	−0.10	0.70±0.14	—	0.69	0.34	—	—
S73	—	—	—	—	—	0.24	—	—
S74	327.53	−0.86	0.74±0.11	115.0 ± 12.0	0.74	0.21	—	—
S76	326.95	0.01	0.44±0.03	66.0 ± 5.0	0.30	0.62	1.99±0.32	—
S79	326.68	0.53	0.51±0.05	—	1.00	0.34	—	—
S91	—	—	—	—	—	0.40	—	—
S92	320.60	0.13	0.35±0.03	171.0 ± 6.0	0.46	0.38	—	—
S96	320.17	0.80	0.45±0.10	—	0.91	0.30	—	—
S97	—	—	—	—	—	0.28	—	—
S104	317.98	−0.76	0.46±0.07	—	0.30	0.55	—	—
S109	—	—	—	—	—	0.53	—	—
S110	—	—	—	—	—	0.57	—	—
S111	—	—	—	—	—	0.35	—	—
S116	314.24	0.43	0.69±0.04	—	0.10	0.32	—	—

Table 4. (Continued)

Name	l_{pp} [°]	b_{pp} [°]	R_{pp}/R	$\theta_{\text{BS-pp}}$ [°]	f_{hot}	$I_{\text{PAH}}/I_{\text{TIR}}$	CV	β_c
S123	312.96	-0.44	0.47±0.06	—	0.35	0.25	—	—
S133	311.47	0.40	0.46±0.07	175.0 ± 12.0	0.92	0.26	—	—
S137	310.99	0.42	0.25±0.04	—	0.64	0.23	—	—
S141	309.55	-0.72	0.06±0.10	—	0.65	0.35	2.20±0.27	—
S143	—	—	—	—	—	0.26	—	—
S150	305.54	0.35	0.23±0.13	—	1.00	0.24	—	—
S156	305.26	0.23	0.33±0.08	—	0.95	0.39	—	—
S163	—	—	—	—	—	0.29	—	—
S181	—	—	—	—	—	0.24	—	—
S186	—	—	—	—	—	0.26	—	—
CN24	—	—	—	—	—	0.28	2.33±0.37	—
CN60	—	—	—	—	—	0.51	—	—
CN63	4.56	-0.13	0.05±0.08	144.0 ± 144.0	0.53	0.41	—	—
CN71	5.89	-0.43	0.50±0.03	—	0.15	0.28	—	—
CN73	6.07	-0.13	0.37±0.08	151.0 ± 16.0	0.52	0.38	—	—
CN88	6.99	-0.28	0.56±0.06	134.0 ± 8.0	0.87	0.26	—	—
CN90	—	—	—	—	—	0.23	—	—
CN99	7.38	0.70	0.64±0.04	158.0 ± 5.0	0.69	0.30	—	—
CN107	—	—	—	—	—	0.37	—	—
CN108	8.12	-0.52	0.30±0.02	—	0.98	0.33	—	—
CN109	—	—	—	—	—	0.43	—	—
CN111	8.32	-0.08	0.27±0.09	47.0 ± 25.0	1.00	0.54	—	—
CN114	8.36	-0.30	0.22±0.11	—	0.98	0.32	—	—
CN138	9.83	-0.71	0.31±0.14	—	0.77	0.29	—	—
CN139	—	—	—	—	—	0.33	—	—
CN148	—	—	—	—	—	0.41	—	—
CS2	359.73	-0.41	0.40±0.07	156.0 ± 14.0	0.67	0.39	—	—
CS33	356.23	0.68	0.42±0.12	139.0 ± 21.0	0.55	0.30	—	—
CS51	354.19	-0.05	0.12±0.07	—	0.47	0.33	—	—
CS57	353.36	-0.16	0.64±0.08	—	0.73	0.28	2.15±0.26	—
CS62	353.09	0.33	0.14±0.05	93.0 ± 28.0	0.47	0.59	—	—
CS79	351.65	0.51	0.52±0.04	—	0.23	0.30	2.18±0.25	—
CS81	—	—	—	—	—	0.51	—	—
E3	—	—	—	—	—	0.21	—	—
E7	74.76	0.62	0.19±0.04	—	0.72	0.24	1.94±0.31	—
E21	82.59	0.38	0.58±0.03	99.0 ± 4.0	0.37	0.30	—	—
E27	90.23	1.74	0.58±0.09	44.0 ± 12.0	0.79	0.31	1.93±0.30	—
E30	—	—	—	—	—	0.32	1.67±0.27	—
E39	106.25	0.97	0.67±0.12	—	0.64	0.12	2.18±0.38	—
E47	114.62	0.23	0.22±0.03	15.0 ± 10.0	0.99	0.19	—	—
E55	133.44	0.07	0.34±0.04	—	0.98	0.26	1.86±0.29	—
E56	134.20	0.81	0.51±0.08	124.0 ± 11.0	0.37	0.26	1.84±0.35	—
E58	—	—	—	—	—	0.35	1.88±0.30	—
E59	—	—	—	—	—	0.23	2.17±0.34	—
E70	—	—	—	—	—	0.24	1.86±0.27	—
E72	182.35	0.21	0.49±0.03	143.0 ± 5.0	0.12	0.22	1.85±0.29	—
E76	190.05	0.48	0.06±0.01	90.0 ± 15.0	0.32	0.26	1.72±0.30	—
E77	196.21	-1.20	0.29±0.06	—	0.82	0.28	1.98±0.30	—

Table 4. (Continued)

Name	l_{pp} [°]	b_{pp} [°]	R_{pp}/R	θ_{BS-pp} [°]	f_{hot}	I_{PAH}/I_{TIR}	CV	β_c
E80	211.87	-1.33	0.46±0.10	117.0 ± 16.0	0.56	0.21		2.10±0.31
E82	212.02	-1.30	0.31±0.01	20.0 ± 3.0	0.96	0.28		1.60±0.28
E83	212.05	-0.74	0.06±0.06	38.0 ± 38.0	0.07	0.22		1.88±0.31
E84	212.41	-1.15	0.26±0.05	61.0 ± 16.0	0.94	0.17		1.99±0.33
E85	217.32	-1.40	0.37±0.04	91.0 ± 8.0	0.91	0.20		1.80±0.31
E86	–	–	–	–	–	0.23		1.74±0.33
E89	–	–	–	–	–	0.21		1.90±0.32
E95	234.77	-0.22	0.22±0.03	108.0 ± 9.0	0.18	0.17		1.81±0.27
E122	–	–	–	–	–	0.51		–
E124	283.94	-0.83	0.65±0.02	93.0 ± 2.0	0.68	0.27		–
E125	284.64	-0.50	0.32±0.11	170.0 ± 28.0	1.00	0.16		2.12±0.32
E127	286.21	-0.16	0.48±0.02	151.0 ± 3.0	0.15	0.33		–
E134	291.05	-0.77	0.79±0.11	–	0.68	0.28		1.94±0.45

References

- Aannestad, P.A. 1975, *ApJ*, 200, 30
- Anderson, L.D., et al. 2012, *A&A*, 542, A10
- Baug, T., Dewangan, L.K., Ojha, D.K., & Ninan, J.P. 2016, *ApJ*, 833, 85
- Benjamin, R.A., et al. 2003, *PASP*, 115, 953
- Chokshi, A., Tielens, A.G.G.M., & Hollenbach, D. 1993, *ApJ*, 407, 806
- Churchwell, E., et al. 2006, *ApJ*, 649, 759
- Churchwell, E., et al. 2007, *ApJ*, 670, 428
- Churchwell, E., et al. 2009, *PASP*, 121, 213
- Csengeri, T., et al. 2014, *A&A*, 565, A75
- Cutri, R.M., et al. 2013, Explanatory Supplement to the AllWISE Data Release Products, Tech. rep.
- Dale, J.E., Bonnell, I.A., & Whitworth, A.P. 2007, *MNRAS*, 375, 1291
- Decataldo, D., Ferrara, A., Pallottini, A., Gallerani, S., & Vallini, L. 2017, *MNRAS*, 471, 4476
- Deharveng, L., et al. 2010, *A&A*, 523, A6
- Desert, F.-X., Boulanger, F., & Puget, J.L. 1990, *A&A*, 237, 215
- Dewangan, L.K., Ojha, D.K., & Zinchenko, I. 2017, *ApJ*, 851, 140
- Draine, B.T., & Li, A. 2007, *ApJ*, 657, 810
- Draine, B.T., et al. 2014, *ApJ*, 780, 172
- Elmegreen, B.G. 1998, in *ASP Conf. Ser.*, 148, *Origins*, ed. C.E. Woodward et al. (San Francisco: ASP), 150
- Fukui, Y., et al. 2016, *ApJ*, 820, 26
- Giannetti, A., et al. 2017, *A&A*, 606, L12
- Griffin, M.J., et al. 2010, *A&A*, 518, L3
- Gritschneider, M., Naab, T., Walch, S., Burkert, A., & Heitsch, F. 2009, *ApJ*, 694, L26
- Güttler, A. 1952, *Annalen der Physik*, 446, 65
- Habe, A., & Ohta, K. 1992, *PASJ*, 44, 203
- Hattori, Y., et al. 2016, *PASJ*, 68, 37
- Hanaoka, M., et al. 2019, *PASJ*, 71, 6
- Hawarth, T.J., et al. 2015, *MNRAS*, 450, 10
- Inoue, T., & Fukui, Y. 2013, *ApJ*, 774, L31
- Ishihara, D., et al. 2010, *A&A*, 514, A1
- Ishihara, D., Kaneda, H., Onaka, T., Ita, Y., Matsuura, M., & Matsunaga, N. 2011, *A&A*, 534, A79
- Jarrett, T.H., et al. 2011, *ApJ*, 735, 112
- Jones, A.P., Tielens, A.G.G.M., & Hollenbach, D.J. 1996, *ApJ*, 469, 740
- Jones, A.P., & Habart, E. 2015, *A&A*, 581, A92
- Jones, A.P., Ysard, N., Köhler, M., Fanciullo, L., Bocchino, M., Micelotta, E., Verstraete, L., & Guillet, V. 2014, *Faraday Discussions*, 168, 313
- Kohno, M., et al. 2018, *PASJ*, arXiv:1809.00118
- Kuan, Y.-J., Mehringer, D.M., & Snyder, L.E. 1996, *ApJ*, 459, 619
- Latter, W.B. 1991, *ApJ*, 377, 187
- Lis, D.C., & Menten, K.M. 1998, *ApJ*, 507, 794
- Mennella, V., Brucato, J.R., Colangeli, L., Palumbo, P., Rotundi, A., & Bussoletti, E. 1998, *ApJ*, 496, 1058
- Micelotta, E.R., Jones, A.P., & Tielens, A.G.G.M. 2010a, *A&A*, 510, A37
- Micelotta, E.R., Jones, A.P., & Tielens, A.G.G.M. 2010b, *A&A*, 510, A36
- Molinari, S., et al. 2010, *PASP*, 122, 314
- Molinari, S., et al. 2016, *A&A*, 591, A149
- Murakami, H., et al. 2007, *PASJ*, 59, S369
- Onaka, T., et al. 2007, *PASJ*, 59, S401
- Pilbratt, G.L., et al. 2010, *A&A*, 518, L1
- Planck Collaboration, et al. 2011, *A&A*, 536, A23
- Poglitsch, A., et al. 2010, *A&A*, 518, L2
- Rapacioli, M., Calvo, F., Spiegelman, F., Joblin, C., & Wales, D.J. 2005, *Journal of Physical Chemistry A*, 109, 2487
- Rodgers, A.W., Campbell, C.T., & Whiteoak, J.B. 1960, *MNRAS*, 121, 103
- Smith, M.W.L., et al. 2012, *ApJ*, 756, 40
- Tabatabaei, F.S., et al. 2014, *A&A*, 561, A95
- Takahira, K., Shima, K., Habe, A., & Tasker, E.J. 2018, *PASJ*, 70, S58
- Tielens, A.G.G.M. 2005, *The Physics and Chemistry of the Interstellar Medium*
- Tielens, A.G.G.M. 2008, *ARA&A*, 46, 289
- Torii, K., et al. 2015, *ApJ*, 806, 7
- Torii, K., et al. 2018a, *PASJ*, arXiv:1706.07164
- Torii, K., et al. 2018b, *PASJ*, 70, S51
- Wickramasinghe, N.C. 1967, *Interstellar grains*
- Wright, E.L., et al. 2010, *AJ*, 140, 1868
- Zinnecker, H., & Yorke, H.W. 2007, *ARA&A*, 45, 481